

# Time-frequency analysis of chaotic systems

C. Chandre<sup>1</sup>, S. Wiggins<sup>2</sup>, T. Uzer<sup>1</sup>

<sup>1</sup>*Center for Nonlinear Science, School of Physics, Georgia Institute of Technology,  
Atlanta, Georgia 30332-0430, U.S.A.*

<sup>2</sup>*Department of Mathematics, University of Bristol, Bristol BS8 1TW, U.K.*

---

## Abstract

We describe a method for analyzing the phase space structures of Hamiltonian systems. This method is based on a time-frequency decomposition of a trajectory using wavelets. The ridges of the time-frequency landscape of a trajectory, also called instantaneous frequencies, enable us to analyze the phase space structures. In particular, this method detects resonance trappings and transitions and allows a characterization of the notion of weak and strong chaos. We illustrate the method with the trajectories of the standard map and the hydrogen atom in crossed magnetic and elliptically polarized microwave fields.

*Key words:* Time-frequency analysis, wavelets, Hamiltonian systems

*PACS:* 05.45.-a, 32.80.Rm

---

## 1 Introduction

The phase space of a typical Hamiltonian system is a mixture of periodic, quasiperiodic and chaotic trajectories, and the stable and unstable manifolds of these trajectories. The analysis of the trajectories of those systems is central to many branches in physics, ranging from celestial mechanics to chemistry. Several methods have been designed to discriminate between regular (periodic or quasiperiodic) and chaotic trajectories. For two degrees of freedom, the most commonly used method is a Poincaré section which is a plane section of the three dimensional energy surfaces. These sections give pictures of phase space and allow to analyze qualitatively the stability properties of the system by revealing, e.g., the invariant tori, the stable islands surrounding elliptic periodic orbits and the spatial extent of chaotic trajectories. However, these sections do not provide very accurate information and the visual inspection of these sections for higher dimensional systems is less straightforward since, e.g., for Hamiltonian systems with three degrees of freedom, these sections are four

dimensional.

Much of our understanding of nonlinear systems is based on their frequencies and especially resonances between them (perturbation theorems, intramolecular dynamics [1,2], Laskar's work in celestial mechanics [3,4,5] and particle accelerators [6]). One way to obtain accurate information on the stability of the system is to associate with a given trajectory an indicator such as a frequency (in general, several indicators are associated with a given trajectory) and construct, e.g., a frequency representation of phase space. In this frequency space, regular regions are characterized by a very small variation of the frequency as the time interval on which this frequency is computed increases (diffusion constant in Laskar's work [7]). The main advantage of this method is that it is generalizable to systems with any number of degrees of freedom [3].

However, a frequency representation of the phase space does not provide the history and the local properties of a trajectory. The computation of asymptotic quantities (such as Lyapunov exponents, entropy or fractal dimensions) does not provide dynamical information. These quantities only reflect the asymptotic behavior of the system. For many purposes infinite-time quantities are not sufficient : rather than knowing whether or not a trajectory is chaotic, it is naturally desirable to say when, where, and to what degree a trajectory is chaotic.

In this article, we describe a method that gives a *time-frequency* representation of trajectories, i.e., that provides dynamical information on the system. The idea is to follow a given trajectory and see if the phase space structures where the trajectory passes by are revealed by analyzing a single trajectory. For quasiperiodic and chaotic systems, time-frequency representation is revealing because it shows when and how motion can be trapped in some resonance zones associated with quasiperiodicity. It also show the degree of chaoticity of some part of phase space visited by the trajectory.

In a nutshell, we associate a set of time-varying frequencies with the trajectory by decomposing it on a set of elementary functions, the wavelets, which are localized in time and frequency. Wavelet decomposition has been used to analyze trajectories of Hamiltonian systems in celestial mechanics [8] and in molecular dynamics [9,10]. In Refs. [8,10], the main frequency was extracted by computing the frequency curve where the modulus of the wavelet transform is maximum. However, stopping at this main frequency can give misleading or wrong information about resonance transitions. Instead, we have found that the relevant information of the trajectory is contained in the *ridges* of the landscape formed by the magnitude of the coefficients of the time-frequency decomposition [11]. A ridge curve (which has a certain time length) corresponds to time-frequency energy localization and is also called *instantaneous frequency* curve. We show that the instantaneous frequencies point to resonance trappings and transitions, and give a clear characterization of the degree of chaoticity.

In Sec. 2, we describe the time-frequency method and the extraction of ridges by two methods: the windowed Fourier transform and the continuous wavelet transform. In Sec. 3, we present briefly the two models which are used to illustrate the method in Sec. 4: the first one is the standard map which is used as a benchmark model for the method since the phase space structures of this model are well-known, and the second one is the hydrogen atom driven by an elliptically polarized microwave field which is a basic and realistic problem in atomic physics with three degrees of freedom.

We show how time-frequency analysis reveals the phase space structures: For two degrees of freedom, we compare this analysis with the Poincaré surface of section, and we show that the time-frequency analysis can be carried out for higher dimensional systems.

In Appendix A, we give an approximation of the ridge curves for a quasiperiodic trajectory and in Appendix B, we compute the effect of finite time on the computation of the ridges.

## 2 Time-frequency analysis

Given a real signal  $f(t)$  which can be, e.g., one coordinate of the system (one position or one momentum for instance), two methods are used to compute a time-frequency (denoted  $u - \xi$ ) representation of  $f$ : windowed Fourier transform and continuous wavelet transform. We assume that we have computed the trajectory for all times  $t \in \mathbb{R}$ . The effect of finite time interval is analyzed in Appendix B. For more details on time-frequency analysis, we refer to Refs. [12,13,11,14,15]

### 2.1 Windowed Fourier transform

The windowed Fourier transform (also called Gabor transform) of  $f(t)$  is given by

$$Sf(u, \xi) = \int_{-\infty}^{+\infty} f(t)g(t - u)e^{-i\xi t} dt, \quad (1)$$

where the window  $g$  is chosen to be a Gaussian window  $g(t) = e^{-t^2/2\sigma^2}/(\sigma^2\pi)^{1/4}$ . We notice that in Laskar's work [3,4], the Hanning filter  $\chi(t) = 1 - \cos(2\pi t/T)$  over a time interval  $[0, T]$ , is chosen rather than a Gaussian filter. The Hanning filter has the advantage of a finite support whereas the Gaussian filter has a minimal time-frequency resolution. We will consider an energy density in the

time-frequency plane called spectrogram

$$P_S f(u, \xi) = |Sf(u, \xi)|^2.$$

We notice that  $P_S f(u, -\xi) = P_S f(u, \xi)$  for  $f$  real. It is thus sufficient to consider the positive frequency part of the time-frequency plane.

### 2.1.1 The algorithm

The algorithm to compute  $Sf(u, \xi)$  uses one fast Fourier transform (FFT) of  $f(\cdot + u)g(\cdot)$  at each time  $u$  since

$$Sf(u, \xi) = e^{-i\xi u} \int_{-\infty}^{+\infty} f(t + u)g(t)e^{-i\xi t} dt.$$

### 2.1.2 Time-frequency resolution

The resolution of the transform is constant in time and in frequency. The time spread around a point  $(u, \xi)$  in the time-frequency plane, defined as

$$\sigma_{time}(u, \xi) = \left( \int_{-\infty}^{+\infty} (t - u)^2 |g_{u,\xi}(t)|^2 dt \right)^{1/2},$$

where  $g_{u,\xi}(t) = g(t - u)e^{-i\xi t}$ , is independent of  $u$  and  $\xi$ . For a Gaussian window  $g(t) = e^{-t^2/2\sigma^2}/(\sigma^2\pi)^{1/4}$ , it is equal to  $\sigma/\sqrt{2}$ . The frequency spread around  $(u, \xi)$  defined as

$$\sigma_{freq}(u, \xi) = \left( \frac{1}{2\pi} \int_{-\infty}^{+\infty} (\omega - \xi)^2 |\hat{g}_{u,\xi}(\omega)|^2 d\omega \right)^{1/2}$$

does not depend on  $u$  and  $\xi$  since  $\hat{g}_{u,\xi}(\omega) = \hat{g}(\omega - \xi)e^{iu(\xi - \omega)}$ . For a Gaussian window, it is equal to  $1/(\sigma\sqrt{2})$ . We notice that the product of the time spread with the frequency spread at a given point  $(u, \xi)$  in the time frequency-plane is constant and larger than  $1/2$  (Heisenberg uncertainty). It is minimum for a Gaussian window.

## 2.2 Continuous wavelet transform

The continuous wavelet transform of  $f(t)$  gives a time-scale representation of the trajectory and is given by

$$Wf(u, s) = \frac{1}{\sqrt{s}} \int_{-\infty}^{+\infty} f(t)\psi^* \left( \frac{t - u}{s} \right) dt, \quad (2)$$

where the mother wavelet  $\psi$  is chosen to be a Gabor (modulated Gaussian) wavelet, also called Morlet-Grossman wavelet:  $\psi(t) = e^{i\eta t} e^{-t^2/2\sigma^2} / (\sigma^2 \pi)^{1/4}$ . The transform depends on  $\eta$  which is the center frequency of the wavelet

$$\eta = \frac{1}{2\pi} \int_{-\infty}^{+\infty} \omega |\hat{\psi}_{u,s}(\omega)|^2 d\omega,$$

where  $\psi_{u,s}(t) = s^{-1/2} \psi[(t-u)/s]$ . The time-frequency representation is obtained by the relation between the scale  $s$  and the frequency  $\xi$ :

$$\xi = \frac{\eta}{s}. \quad (3)$$

We will consider the normalized scalogram

$$P_W f(u, \xi = \eta/s) = \frac{1}{s} |Wf(u, s)|^2,$$

which can be interpreted as the energy density in the time-frequency plane. Again, we notice that  $P_W f(u, -\xi) = P_W f(u, \xi)$ . For the computation of the wavelet decomposition, we only consider the positive frequency part of the time-frequency plane.

### 2.2.1 The wavelet algorithm

In order to use a fast wavelet algorithm, we consider that  $f$  and  $\psi$  are periodic (and hence  $Wf(u, s)$  is periodic in the variable  $u$ ) with period  $T$ , the time span of the trajectory. By taking the Fourier transform of Eq. (2), one has:

$$\hat{W}f(\omega, s) = \sqrt{s} \hat{f}(\omega) \hat{\psi}^*(s\omega),$$

Since  $\hat{\psi}(\omega)$  is known exactly, one has to compute  $\hat{f}$  by FFT and then retrieve  $Wf$  by an inverse FFT. For this computation, the scales are chosen according to a dyadic sampling  $s_{i,j} = 2^{i+j/n} T/N$  for  $i = 1, \dots, m$  and  $j = 1, \dots, n$  where  $m$  is the number of octaves,  $n$  is the number of voices per octave and  $N$  is the number of points in the time series on the interval  $[0, T]$ . The relative error produced by the algorithm on the computation of the frequency is then  $\Delta\omega/\omega = 1 - 2^{-1/n} \approx (\log 2)/n$ . This error decreases when the number of voices per octave is increased. We chose  $n \approx 300$  in our computations (which gives a relative error of  $2 \cdot 10^{-3}$ ). In what follows, we choose  $m = \log_2 N - 3$  where  $N$  is the total number of points in the series.

In order to compute the continuous wavelet transform, we use the routines of WAVELAB, written in MATLAB [16].

*Remark:* In practice we choose  $\eta = 2$  and  $\sigma = 6$ . We notice that the wavelet does not satisfy the admissibility condition  $\hat{\psi}(0) = 0$  which is required for

reconstructing the trajectory. However  $\hat{\psi}(0) = (4\pi\sigma^2)^{1/4}e^{-\sigma^2\eta^2/2}$  is negligible since  $\sigma\eta$  is large enough (e.g, if  $\sigma\eta = 12$ ,  $|\hat{\psi}(0)| < 10^{-30}$ ). If one wants to satisfy the admissibility condition, the wavelet has to be chosen according to

$$\psi(t) = ce^{-t^2/(2\sigma^2)}(e^{i\eta t} - e^{-\sigma^2\eta^2/2}),$$

with  $c = (\pi\sigma^2)^{-1/4}(1 - 2e^{-3\sigma^2\eta^2/4} + e^{-\sigma^2\eta^2})^{-1/2}$ . The relation between the scale and the frequency is changed. It becomes  $\xi = (1 + e^{-\sigma^2\eta^2})\eta/s$  up to the first order. For the parameters we choose, this error in determining the frequency is negligible.

### 2.2.2 Time-frequency resolution

The time-frequency resolution depends on the scale of the wavelet. The time spread around a point  $(u, s)$  in the time-scale plane, defined as

$$\sigma_{time}(u, s) = \left( \int_{-\infty}^{+\infty} (t - u)^2 |\psi_{u,s}(t)|^2 dt \right)^{1/2},$$

is independent of  $u$  (the moment of observation of the frequency content) and is proportional to the scale  $s = \eta/\xi$  for a mother wavelet of the form  $\psi(t) = e^{i\eta t}g(t)$ . For a Gabor wavelet,  $\sigma_{time}$  is equal to  $\sigma\eta/(\sqrt{2}\xi)$ . From this equation, we see that for low frequency the time spread of the wavelet is large, whereas for high frequencies, it is small. This allows a more accurate computation of the frequency since for low frequencies a larger time interval is needed (large enough to contain several oscillations at that frequency). Increasing the parameters  $\sigma$  and  $\eta$  increases the time spread which varies as  $1/\xi$ . The frequency spread around  $\xi = \eta/s$  defined as

$$\sigma_{freq}(u, s) = \left( \frac{1}{2\pi} \int_{-\infty}^{+\infty} (\omega - \eta/s)^2 |\hat{\psi}_{u,s}(\omega)|^2 d\omega \right)^{1/2},$$

is independent of  $u$  and is linearly dependent on the frequency for a mother wavelet of the form  $\psi(t) = e^{i\eta t}g(t)$ . For a Gabor wavelet,  $\sigma_{freq}$  is equal to  $\xi/(\sigma\eta\sqrt{2})$ . We notice that the product of the time spread with the frequency spread at a given time-frequency point is independent of  $u$  and  $\xi = \eta/s$  and is larger than  $1/2$  (Heisenberg uncertainty). The Heisenberg uncertainty is minimum for the Gabor wavelet. Increasing or decreasing the product of the parameters  $\sigma\eta$  is a compromise between the time resolution and the frequency resolution.

### 2.3 Differences between windowed Fourier transform and wavelet transform

Both methods have time-frequency resolution limitations for the determination of the instantaneous frequencies. The windowed Fourier transform relies on an a priori choice of length of the window  $\sigma$ . Any event (trapping, transition, etc.) happening on short time-scales (less than  $\sigma$ ) or with small frequencies (less than  $\sigma^{-1}$ ) is missed by this method. On the contrary, the main advantage of the wavelet method is that it follows the rapid variations of the instantaneous frequencies since it adapts the length of the window according to the frequency [12].

For quasiperiodic trajectories, there are practically no differences between both methods. However, for chaotic trajectories where variations of frequency with respect to time are expected, the wavelet basis is more adapted since it leads to a better time-frequency resolution. In what follows, we choose the wavelet basis in order to compute the time-frequency content of the trajectories.

### 2.4 Ridge plots

The different main frequencies of the trajectory can be obtained by looking at the *ridges* of the spectrogram or normalized scalogram, also called *instantaneous frequencies*. These ridges are local maxima with respect to the frequency  $\xi$ , of the energy density in the time-frequency plane which is the spectrogram or the normalized scalogram.

For a periodic trajectory  $f(t) = e^{i\omega t}$ , the spectrogram

$$P_S f(u, \xi) = 2\sigma\sqrt{\pi}e^{-\sigma^2(\omega-\xi)^2}$$

and the normalized scalogram

$$P_W f(u, \xi) = 2\sigma\sqrt{\pi}e^{-\sigma^2\eta^2(\omega/\xi-1)^2}$$

are maximum for  $\xi = \omega$ , independently of the time  $u$ . Therefore, the ridge plot will present a single flat ridge located at  $\xi = \omega$ .

For a quasi-periodic trajectory  $f(t) = \sum_k A_k e^{i\omega_k t}$ , the spectrogram and the normalized scalogram present a sum of localized peaks and interference terms : The wavelet transform of  $f$  is given by the sum of the wavelet transform of  $A_k e^{i\omega_k t}$  since the wavelet transform is linear. Therefore, the normalized scalogram is a sum of peaks located at  $\xi = \omega_k$  and of width proportional to  $\omega_k/(\eta\sigma)$ , with some additional interference terms of the form

$$I_{kl} = A_l A_k^* e^{-\sigma^2\eta^2(\omega_l/\xi-1)^2/2} e^{-\sigma^2\eta^2(\omega_k/\xi-1)^2/2} e^{i(\omega_l-\omega_k)u}.$$

The effect of these terms is visible if (a) at least two amplitudes  $A_k$  and  $A_l$  are large enough, and (b) if the difference of their frequencies  $\omega_l - \omega_k$  is smaller than

$\omega_l/(\eta\sigma)$  (see Appendix A). In order to distinguish two frequency components  $\omega_l$  and  $\omega_k$  of amplitude  $A_k$  and  $A_l$  of the same order, the parameters of the wavelet must be chosen according to the condition  $\eta\sigma \geq (\omega_l + \omega_k)/|\omega_l - \omega_k|$ . The time-frequency landscape has *approximately* a set of flat ridges (if the interferences are negligible) at  $\xi = \omega_k$ .

*Remark: Laskar's frequency map analysis.* In order to determine accurately the frequencies of a quasiperiodic trajectory and the location of the ridges, we use Laskar's frequency map analysis [3,7,4] which is a Fourier based analysis of quasiperiodic functions  $f(t) = \sum_k a_k e^{i\omega_k t}$  known on a finite interval  $[0, T]$ . The approximation of the main frequency  $\omega_1$ , called  $\omega'_1$  is obtained by maximizing the modulus of

$$\phi(\omega) = \langle f, e^{i\omega t} \rangle = \frac{1}{T} \int_0^T f(t) \chi(t) e^{-i\omega t},$$

where  $\chi(t) = 1 - \cos(2\pi t/T)$  is a Hanning filter. The amplitude  $a'_1$  of the component with frequency  $\omega'_1$  is obtained by projection on  $e^{i\omega'_1 t}$ . Laskar proved that this method gives the main frequency with an accuracy of order  $T^{-4}$  [4] (i.e.,  $\omega'_1 - \omega_1 = O(T^{-4})$ ) instead of an ordinary Fourier transform which gives an accuracy of order  $T^{-1}$ . The approximation of the next frequency  $\omega_2$  is obtained by iterating the above procedure using  $f_1(t) = f(t) - a'_1 e^{i\omega'_1 t}$ . Since the basis  $\{e^{i\omega'_k t}\}$  is not orthogonal for the scalar product  $\langle \cdot, \cdot \rangle$ , a Gramm-Schmidt orthogonalization is necessary to obtain the next frequencies  $\omega'_k$  for  $k \geq 3$ .

For a chaotic trajectory, a ridge is a curve or a segment of curve  $\xi_{loc}(u)$  in the time-frequency plane which is at each time  $u$  a local maximum of the normalized scalogram, i.e.,

$$\left. \frac{\partial}{\partial \xi} P_W f(u, \xi) \right|_{\xi=\xi_{loc}(u)} = 0,$$

$$\left. \frac{\partial^2}{\partial \xi^2} P_W f(u, \xi) \right|_{\xi=\xi_{loc}(u)} < 0.$$

Each ridge has a weight which is the value of the normalized scalogram on this ridge (it varies continuously in time). We will refer this value as the amplitude of the ridge. We call main ridge or main frequency, the ridge  $\xi_m(u)$  (or a set of ridges) where the normalized scalogram is maximum:

$$P_W f(u, \xi_m(u)) = \max_{\xi} P_W f(u, \xi).$$

In what follows, we will detect ridges by analyzing one coordinate of the system. We will show that the set of ridges of one coordinate contains all the frequency content of the trajectory, that is to say, the ridge plot will not be dependent on the choice of the coordinate used for the computation of the time-frequency transform. The respective amplitudes of the ridges depend on



the specific coordinate chosen for the computation of the normalized scalogram. For instance, the main ridge depends in general on the chosen coordinate whereas the ridge plot does not.

*Detection of the ridges.* For each time  $u$ , we are searching for the *local* maxima of the spectrogram or the normalized scalogram. In general, there is an infinite number of these ridges. We only detect the ones with sufficient amplitude according to a threshold  $\epsilon$ , i.e., we determine the set of ridges  $\xi_{loc}(u)$  such that

$$P_W f(u, \xi_{loc}) \geq \epsilon \max_{\xi} P_W f(u, \xi).$$

### 3 Models

The time-frequency analysis can be performed on trajectories of maps or of flows. In this section, we illustrate the time-frequency analysis on the two models: the well-known standard map and the hydrogen atom in crossed magnetic and elliptically polarized microwave field.

The standard map is a two-dimensional area-preserving map  $(x, y) \mapsto (x', y')$  :

$$x' = x - a \sin y \tag{4}$$

$$y' = x' + y \pmod{2\pi}. \tag{5}$$

This example provides a benchmark for the time-frequency analysis since the phase space structures are well-known in this example.

The hydrogen atom driven by a elliptically polarized microwave field (polarized in the orbital plane) and a constant magnetic field perpendicular to the orbital plane is described by the following Hamiltonian [17]:

$$H(x, y, p_x, p_y, t) = \frac{p_x^2 + p_y^2}{2} - \frac{1}{\sqrt{x^2 + y^2}} + V_F(x, y, \omega t) + V_B(x, y, p_x, p_y), \tag{6}$$

where  $V_F$  is the contribution of the elliptically polarized microwave field and  $V_B$  is the one of the magnetic field :

$$V_F(x, y, \omega t) = F(x \cos \omega t + \alpha y \sin \omega t),$$

$$V_B(x, y, p_x, p_y) = \frac{B}{2}(xp_y - yp_x) + \frac{B^2}{8}(x^2 + y^2),$$

where  $\omega$  is the frequency of the microwave field and  $\alpha$  is the ellipticity degree. For  $\alpha = 0$ , the microwave field is linearly polarized (along the  $x$  direction), and for  $\alpha = 1$ , it is circularly polarized. In the circularly polarized case, the problem has two effective degrees of freedom. For  $\alpha \in ]0, 1[$ , the field is elliptically polarized and is a three degree of freedom problem.

The magnetic field  $B$  perpendicular to the orbital plane of the electron limits the diffusion of trajectories [18,19]. With it in place, trajectories will stay for a longer time close to the nucleus before ionizing, allowing longer trajectories to analyze by time-frequency analysis.

*Rescaling of the Hamiltonian:* By rescaling positions, momenta and time, we can assume that  $\omega = 1$ . The rescaling of time is obtained by considering the Hamiltonian  $\omega^{-1}H(x, y, p_x, p_y, t/\omega)$  where  $H(x, y, p_x, p_y, t)$  is Hamiltonian (6). Then we rescale positions and momenta :  $x' = \omega^{2/3}x$ ,  $p'_x = \omega^{-2/3}p_x$ ,  $y' = \omega^{2/3}y$  and  $p'_y = \omega^{-2/3}p_y$ , which is a canonical transformation generated by  $S(x', y', p_x, p_y) = -\omega^{-2/3}(x'p_x + y'p_y)$ . Then we rescale the momenta by changing  $H$  into  $\omega^{1/3}H(\omega^{-1/3}p_x, \omega^{-1/3}p_y, x, y)$ . We notice that this transformation does not change the equations of motion. The resulting Hamiltonian is the same as Hamiltonian (6) with  $\omega = 1$  and a rescaled value for the amplitude of the microwave field and the magnetic field: The amplitude of the microwave field is rescaled as  $F' = F\omega^{-4/3}$  and the magnetic field as  $B' = B/\omega$ . In what follows, we assume that  $\omega = 1$ .

### 3.1 Semi-parabolic coordinates

The singularity of the potential in Hamiltonian (6) is removed by changing the coordinates to the semi-parabolic coordinates and a nonlinear change of time. We perform the canonical transformation generated by

$$S(u, v, p_x, p_y) = -\frac{u^2 - v^2}{2}p_x - uvp_y.$$

The expression of the old coordinates as functions of the new coordinates is

$$\begin{aligned} x &= \frac{u^2 - v^2}{2}, \\ y &= uv, \\ p_x &= \frac{up_u - vp_v}{u^2 + v^2}, \\ p_y &= \frac{vp_u + up_v}{u^2 + v^2}. \end{aligned}$$

The Hamiltonian becomes

$$\begin{aligned} H &= \frac{p_u^2 + p_v^2}{2(u^2 + v^2)} - \frac{2}{u^2 + v^2} + F \left( \frac{u^2 - v^2}{2} \cos t + \alpha uv \sin t \right) \\ &\quad + \frac{B}{4}(up_v - vp_u) + \frac{B^2}{32}(u^2 + v^2)^2. \end{aligned} \quad (7)$$

We consider  $t$  as a new variable  $w$  with conjugate momentum  $p_w$ . The new Hamiltonian becomes time-independent:

$$H' = \frac{p_u^2 + p_v^2}{2(u^2 + v^2)} + p_w - \frac{2}{u^2 + v^2} + F \left( \frac{u^2 - v^2}{2} \cos w + \alpha uv \sin w \right) + \frac{B}{4}(up_v - vp_u) + \frac{B^2}{32}(u^2 + v^2)^2.$$

We denote  $E$  the energy of the system described by  $H'$  (which is conserved since  $H'$  does not depend on time). Then we change time by multiplying the Hamiltonian by  $u^2 + v^2$ . The new time  $\tau$  satisfies  $dt/d\tau = u^2 + v^2$  (see Ref. [20]). We consider the effective Hamiltonian whose equations of motions are the same as the ones of Hamiltonian (7):

$$H_{eff} = \frac{p_u^2 + p_v^2}{2} + (p_w - E)(u^2 + v^2) - 2 + F(u^2 + v^2) \left( \frac{u^2 - v^2}{2} \cos w + \alpha uv \sin w \right) + \frac{B}{4}(u^2 + v^2)(up_v - vp_u) + \frac{B^2}{32}(u^2 + v^2)^3,$$

where  $H_{eff} = 0$ . We shift the momentum  $p_w$  by a factor  $-E$  and the effective Hamiltonian becomes

$$H_{eff} = \frac{p_u^2 + p_v^2}{2} + p_w(u^2 + v^2) - 2 + F(u^2 + v^2) \left( \frac{u^2 - v^2}{2} \cos w + \alpha uv \sin w \right) + \frac{B}{4}(u^2 + v^2)(up_v - vp_u) + \frac{B^2}{32}(u^2 + v^2)^3, \quad (8)$$

We perform the following rotation of coordinates:

$$\begin{aligned} \tilde{u} &= u \cos \frac{w}{2} + v \sin \frac{w}{2}, \\ \tilde{v} &= -u \sin \frac{w}{2} + v \cos \frac{w}{2}, \\ \tilde{w} &= w, \end{aligned}$$

which is a canonical transformation generated by

$$S(\tilde{u}, \tilde{v}, \tilde{w}, p_u, p_v, p_w) = -p_u[\tilde{u} \cos(\tilde{w}/2) - \tilde{v} \sin(\tilde{w}/2)] - p_v[\tilde{u} \sin(\tilde{w}/2) + \tilde{v} \cos(\tilde{w}/2)] - \tilde{w}p_w.$$

The Hamiltonian (8) becomes

$$\begin{aligned}
\tilde{H}_{eff} &= \frac{\tilde{p}_u^2 + \tilde{p}_v^2}{2} + \tilde{p}_w(\tilde{u}^2 + \tilde{v}^2) - 2 \\
&\quad - \frac{1}{2} \left(1 - \frac{B}{2}\right) (\tilde{u}^2 + \tilde{v}^2)(\tilde{u}\tilde{p}_v - \tilde{v}\tilde{p}_u) + \frac{F}{2}(\tilde{u}^4 - \tilde{v}^4) \\
&\quad + (\alpha - 1)F(\tilde{u}^2 + \tilde{v}^2) \left[ \frac{\tilde{u}^2 - \tilde{v}^2}{2} \sin \tilde{w} + \tilde{u}\tilde{v} \cos \tilde{w} \right] \sin \tilde{w} \\
&\quad + \frac{B^2}{32}(\tilde{u}^2 + \tilde{v}^2)^3, \tag{9}
\end{aligned}$$

where  $\tilde{H}_{eff}$  is still equal to zero. In the circularly polarized case ( $\alpha = 1$ ), the above Hamiltonian is independent of  $\tilde{w}$ , thus  $\tilde{p}_w$  is constant, i.e.,  $p_w + (up_v - vp_u)/2 = const$ . Thus the circularly polarized problem has two degrees of freedom. Poincaré surfaces of section will be drawn: the surfaces are the ones with  $\tilde{P}_\rho = 0$  (in the rotating frame), i.e.,  $\tilde{u}\tilde{p}_u + \tilde{v}\tilde{p}_v = 0$ .

### 3.2 Choice of initial conditions

We choose the initial conditions for the circularly polarized problem. Given the values of  $F$  and  $B$ , the energy of the system is chosen according to Ref. [18] in the maximum configuration. At this energy, there is a stationary point of the flow and interesting dynamics happens in this case (see Ref. [18] for more details). We notice that the stationary points belong to the surface  $\tilde{P}_\rho = 0$ . The maximum configuration is obtained for  $\tilde{v} = 0$ , i.e. for

$$\tilde{p}_w = \frac{3}{8}(1 - B)u_0^4 - Fu_0^2, \tag{10}$$

where  $u_0$  is the positive real solution of

$$\frac{1}{2}(1 - B)u_0^6 - Fu_0^4 - 4 = 0.$$

We notice that the equation that determines  $u_0^2$  has always one positive real root and two complex conjugated roots for  $F > 0$  and  $B < 1$ .

Once we have fixed  $F$ ,  $B$  and the energy of the system  $p_w$ , we compute Poincaré sections by the following procedure. These surfaces will be in the  $(x, y)$ -plane. We consider one point  $(x, y)$  on this plane. We compute the associated  $\tilde{u}$  and  $\tilde{v}$ :

$$\begin{aligned}\tilde{u} &= \left(\sqrt{x^2 + y^2} + x\right)^{1/2}, \\ \tilde{v} &= (\text{sgn } y) \left(\sqrt{x^2 + y^2} - x\right)^{1/2}.\end{aligned}$$

The following conditions  $\tilde{u}\tilde{p}_u + \tilde{v}\tilde{p}_v = 0$  (which is  $\tilde{P}_\rho = 0$ ) and  $\tilde{H}_{eff}(\tilde{u}, \tilde{v}, \tilde{p}_u, \tilde{p}_v) = 0$  determine  $\tilde{p}_u$  and  $\tilde{p}_v$ :

$$\begin{aligned}\tilde{p}_u &= -\frac{\tilde{v}}{2} \left[ \left(1 - \frac{B}{2}\right) (\tilde{u}^2 + \tilde{v}^2) + \varepsilon\delta(\tilde{u}, \tilde{v}) \right], \\ \tilde{p}_v &= \frac{\tilde{u}}{2} \left[ \left(1 - \frac{B}{2}\right) (\tilde{u}^2 + \tilde{v}^2) + \varepsilon\delta(\tilde{u}, \tilde{v}) \right],\end{aligned}$$

where

$$\delta(\tilde{u}, \tilde{v}) = \left[ (1 - B)(\tilde{u}^2 + \tilde{v}^2)^2 - 8\tilde{p}_w - 4F(\tilde{u}^2 - \tilde{v}^2) + 16(\tilde{u}^2 + \tilde{v}^2)^{-1} \right]^{1/2},$$

and  $\varepsilon = \pm 1$  depending on whether we specify the trajectory crossing the Poincaré section  $\tilde{P}_\rho = 0$  in one direction ( $\dot{\tilde{P}}_\rho > 0$ ) or the other ( $\dot{\tilde{P}}_\rho < 0$ ). We use Poincaré sections in order to exhibit phase space structures and show that the time-frequency analysis of chaotic trajectories is able to reveal these structures.

## 4 Illustration of the time-frequency method

In what follows, we consider the trajectories of the standard map (discrete time) and the trajectories of the hydrogen atom in crossed fields (continuous time). We will show that the phase space structures encountered by a trajectory are revealed by the time-frequency analysis of a single coordinate of this trajectory, i.e., by the computation of the ridges of the time-frequency landscape, the instantaneous frequencies.

We compute the time-frequency content of real time series (e.e., one coordinate of the system) obtained by iterating the map or integrating the flow. We only compute the time-frequency content of the trajectory in the positive frequency region.

### 4.1 Trajectories of the Standard Map

#### 4.1.1 Quasiperiodic trajectory

We consider a trajectory of the standard map for  $K = 0.9710$  starting at  $x_0 = 4.176562$  and  $y_0 = 0$  over a time span of 512 iterations (which corresponds

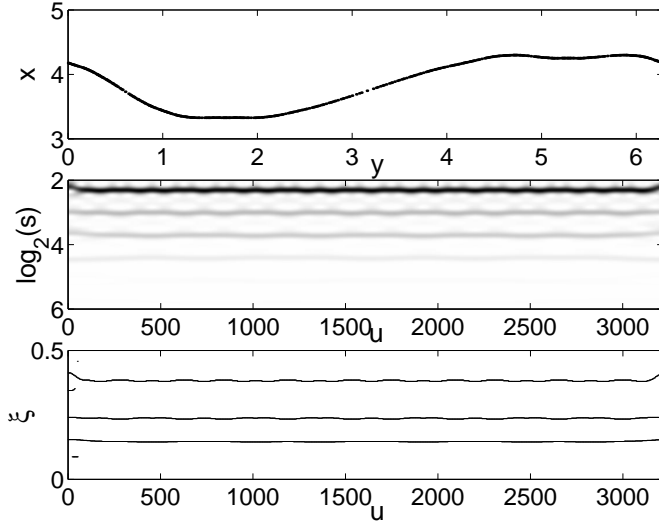


Fig. 1. Phase portrait (first panel), normalized scalogram (second panel) and ridge plot (third panel) of a quasiperiodic trajectory of the standard map obtained for  $K = 0.971$  and initial conditions  $x_0 = 4.176562$  and  $y_0 = 0$ .

to  $T = 3217$  for the corresponding flow). This trajectory, plotted in the first panel of Fig. 1, corresponds to the invariant torus (golden mean torus) whose break-up is studied in Ref. [21] using frequency map analysis. The second panel of Fig. 1 depicts the normalized scalogram in the time-scale plane, i.e. the amplitude of the wavelet coefficients, obtained from the  $x$  coordinate. From this time-scale (or time-frequency) landscape, we extract the local maxima which define the ridges or the instantaneous frequencies of the trajectory. The third panel of Fig. 1 shows the different ridges of the normalized scalogram (the ridge detection threshold is  $\epsilon = 0.1$ ). These ridges are approximately constant in time as one expects. The upper curve represents the main frequency  $\omega_0 = (3 - \sqrt{5})/2$ . The other two main frequency curves in the ridge plot are located at  $\omega_1 = 1 - 2\omega_0$  and  $\omega_2 = 3\omega_0 - 1$ . For a system with two degrees of freedom, there are at most two independent frequencies: in this case, they are equal to  $\omega_0$  and 1 which is the natural frequency for constructing the Poincaré map from the flow (kicked rotor). Each ridge (a priori an infinite number) is a combination of these two frequencies.

We can also see the interferences (oscillations around the expected frequency) between these frequencies. In order to reduce these oscillations, we can increase the parameter  $\eta\sigma$ . We notice that the amplitudes or frequencies of these oscillations do not depend on the length of the time interval in which the trajectory is computed (see Appendix A).

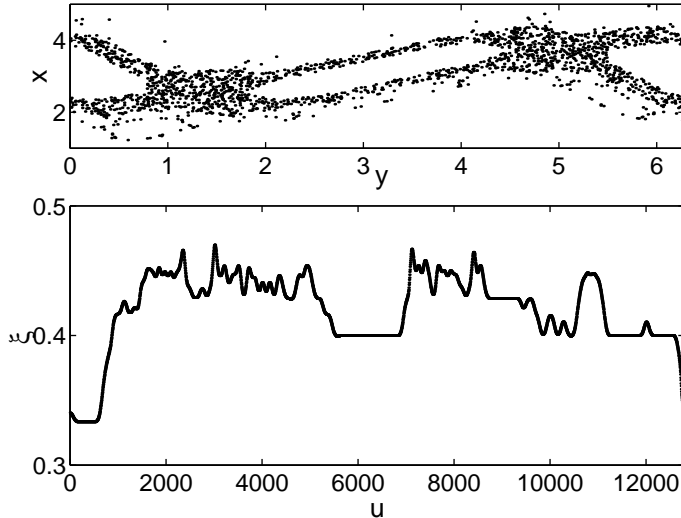


Fig. 2. Phase portrait (first panel) and ridge plot (second panel) of a weakly chaotic trajectory of the standard map obtained for  $K = 1.2$  and initial conditions  $x_0 = 2.5$  and  $y_0 = \pi$ .

#### 4.1.2 Weakly chaotic motion

We consider a trajectory obtained for the standard map with  $K = 1.2$  and initial conditions  $x_0 = 2.5$  and  $y_0 = \pi$ . We analyze this weakly chaotic trajectory over the time interval of total length  $T = 12868$ . The upper panel of Fig. 2 depicts this trajectory. The lower panel depicts the main ridge (the ridge detection threshold is  $\epsilon = 0.5$ ) and shows clearly different trappings as time evolves: trappings in the resonance 1:3 for  $150 \leq t \leq 500$ , in 2:5 for  $5600 \leq t \leq 6800$ , in 4:7 for  $8700 \leq t \leq 9300$ , and in 3:5 for  $11200 \leq t \leq 12600$ . These trappings result from the trajectory passing nearby islands surrounding elliptic periodic orbits (the other ridges contain the secondary frequencies of the nearby quasiperiodic motion). The transitions between these resonances occur quite smoothly, passing by other resonance trappings. They occur when the chaotic trajectory passes nearby hyperbolic periodic orbits where great variations of the frequencies are expected. The trajectory is weakly chaotic since the main information can be obtained from a single instantaneous frequency curve. In this regime, looking at the frequency where the spectrogram or scalogram is maximum (main instantaneous frequency) is meaningful.

#### 4.1.3 Resonance transitions

The time-frequency resolution of wavelets allows us to analyze the mechanism of resonance transition. Figure 3 shows the normalized scalogram in the time-scale plane and the ridge plot (with ridge detection threshold  $\epsilon = 0.1$ ) obtained for the  $x$  coordinate of a trajectory of the standard map with  $K = 1.5$  and initial conditions  $x_0 = 1.35$  and  $y_0 = 0$  on a time interval  $[1700, 2500]$ . In this

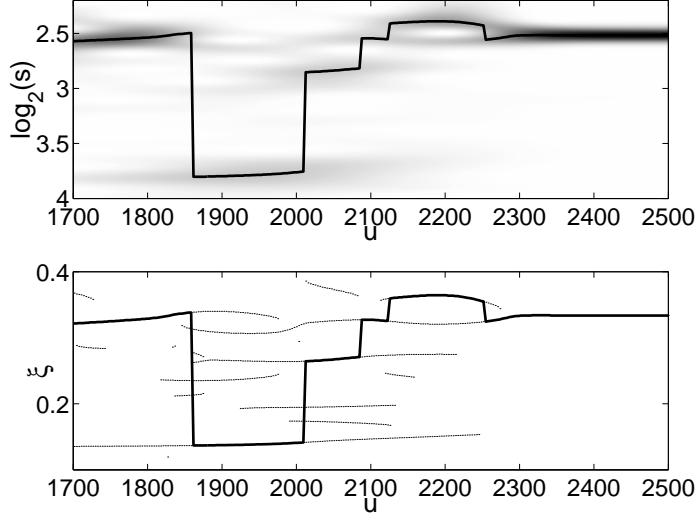


Fig. 3. Ridge plot of the  $x$  component of the trajectory of the standard map with  $K = 1.5$  and initial conditions  $x_0 = 1.35$  and  $y_0 = 0$  on the time interval  $[1700, 2500]$ . The upper panel is the time-scale plane and the lower panel is the ridge plot. The bold line denotes the main frequency curve.

figure, the bold curve represents the main ridge or the main frequency (i.e. where the normalized scalogram is maximum, see Sec. 2.4).

In this time interval, several transitions occur. For instance around  $t = 1860$ , the main frequency jumps discontinuously from the ridge located around  $\omega_1 \approx 0.33$  to the ridge located around  $\omega_2 \approx 0.136$ . One could wrongly conclude that a sharp resonance transition occurred in the system. By looking at secondary ridges, i.e. the ridges with smaller amplitudes than the main frequency, one can see that both ridges existed before and after  $t = 1860$ ; Nothing discontinuous happens in the system. From the ridge plot, the mechanism of resonance transition appears to be the following one: A second ridge at  $\xi = \omega_2$  increases in amplitude from  $t = 1700$  to  $t = 1860$  while the first ridge at  $\xi = \omega_1$  decreases in amplitude. On some time interval (from  $t = 1800$  to  $t = 2000$ ), several ridges of the same order in amplitude appear. At  $t = 1860$ , the second ridge becomes the main frequency. This situation is typical from other ridge plots of trajectories showing transitions from ridges and hence resonance transitions (see Fig. 12). Thus we have a new characterization of resonance transition that applies in more general situations. Resonance transitions are a manifestation of the fulfillment of the Chirikov resonance overlap criterion [22].



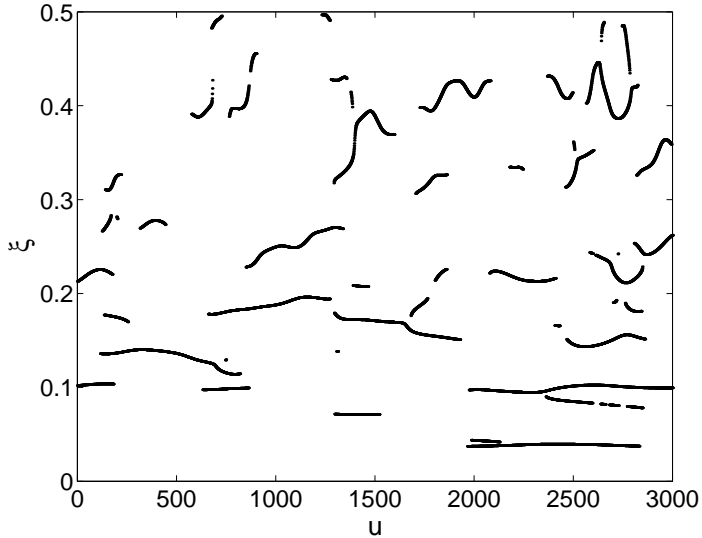


Fig. 4. Ridge plot of a strongly chaotic trajectory of the standard map with  $K = 5$  and initial conditions  $x_0 = 0.95$  and  $y_0 = 0$ .

#### 4.1.4 Strongly chaotic motion

When  $K$  increases, the trajectories are increasingly chaotic (filling a bigger part of phase space). More and more short ridges appear, and in those cases, looking at the main frequency leads to erroneous results as shown above since several ridges have the same amplitude. The time-frequency information cannot be reduced to (or deduced from) a single instantaneous frequency. For instance, the main frequency curve could follow a short flat ridge and one could wrongly deduce a trapping region. We consider a strongly chaotic trajectory of the standard map obtained with  $K = 5$  and initial conditions  $x_0 = 0.95$  and  $y_0 = 0$ . Figure 4 shows the ridge plot obtained from the normalized scalogram (with a ridge detection threshold  $\epsilon = 0.5$ ). It shows that no trappings occur in this time interval. The presence of a lot (but a finite number) of ridges reflects the broad-band spectrum of a chaotic trajectory. These pictures lead to a characterization of weak and strong chaos by looking at the number of important ridges in the system: Weak chaos is characterized by one main connected instantaneous frequency curve whereas strong chaos is characterized by multiple short ridges (the number of them increases as  $K$  increases).

## 4.2 Hydrogen atom in crossed fields

We consider in this section the trajectories of the Hamiltonian flow of the hydrogen atom driven by crossed magnetic and elliptically polarized microwave field in the rotating frame represented by Hamiltonian (9) in the maximum configuration.

Otherwise specified, we consider in this section the following values for the

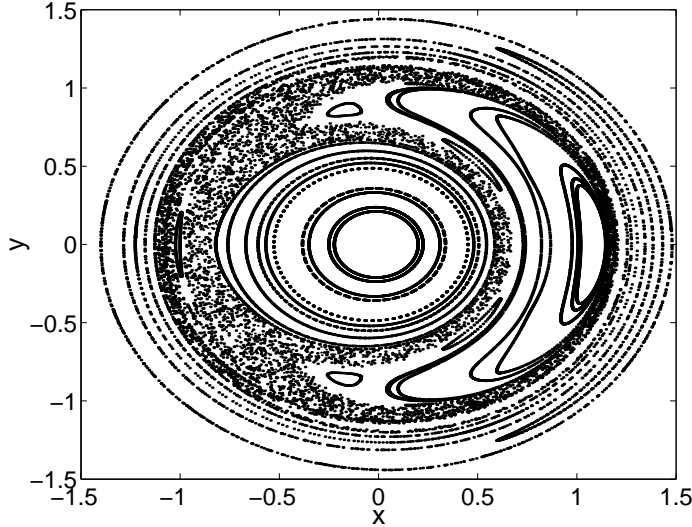


Fig. 5. Poincaré section of the Hamiltonian (9) in the maximum configuration for  $F = 0.015$  and  $B = 0.3$ .

parameters:  $F = 0.015$  and  $B = 0.3$ . Figure 5 depicts a Poincaré section of the Hamiltonian in the circularly polarized case. We analyze the trajectories by applying the wavelet transform on one real coordinate  $x(t)$  or  $y(t)$ .

#### 4.2.1 Periodic orbit

We consider a closed trajectory in phase space obtained for initial conditions  $(x, y) \approx (0.4835, 0.5335)$  in the Poincaré section. A projection of this periodic orbit on the plane  $(x, y)$  is shown in the upper part of Fig. 6. The ridge plot of this orbit is depicted in the lower panel of Fig. 6.

The ridge plot displays only one flat ridge located at the value of its frequency  $\omega_A \approx 0.2952$ . The harmonics are not visible on the ridge plot since these ridges are too small compared to the main ridge (ridge detection threshold  $\epsilon = 0.1$ ). The bumps at  $u = 0$  and  $u = 4500$  are a consequence of the finite time interval on which the periodic trajectory is computed. This effect is discussed in Appendix B.

There are other elliptic periodic orbits in the system: For instance, the one obtained from the initial conditions in the Poincaré section  $(x, y) = (-1.014, 0)$  with frequency  $\omega_B \approx 0.3033$ , and for  $(x, y) = (-0.807, 0.558)$  with frequency  $\omega_C \approx 0.2260$ .

#### 4.2.2 Quasiperiodic trajectory

The ridge plot of a quasiperiodic orbit obtained for initial conditions  $(x, y) = (0.7, 0.5)$  is depicted in Fig. 7. It displays a set of three main ridges around  $\omega_1 \approx 0.17$ ,  $\omega_2 \approx 0.25$  and  $\omega_3 \approx 0.34$  (with a ridge detection threshold  $\epsilon = 0.1$ ). The

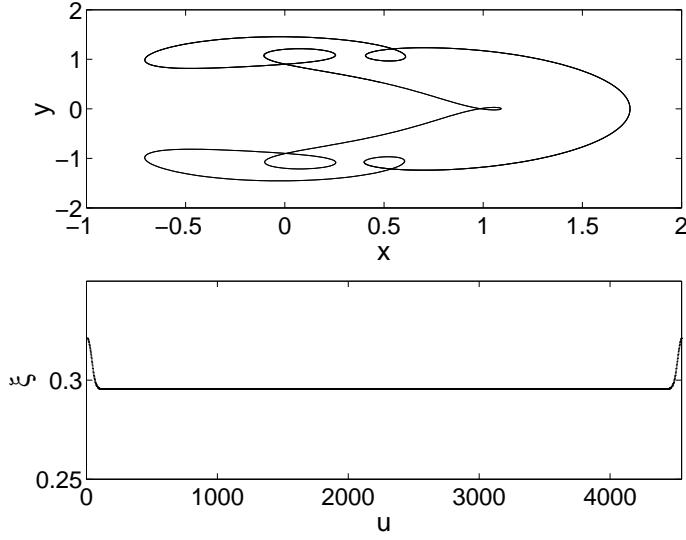


Fig. 6. Ridge plot of a periodic orbit of Hamiltonian (9) for  $F = 0.015$  and  $B = 0.3$  in the maximum configuration obtained for initial conditions  $(x, y) = (0.4835, 0.5335)$  in the Poincaré section. The upper part of the figure represents a projection of the periodic orbit on the  $x - y$  plane.

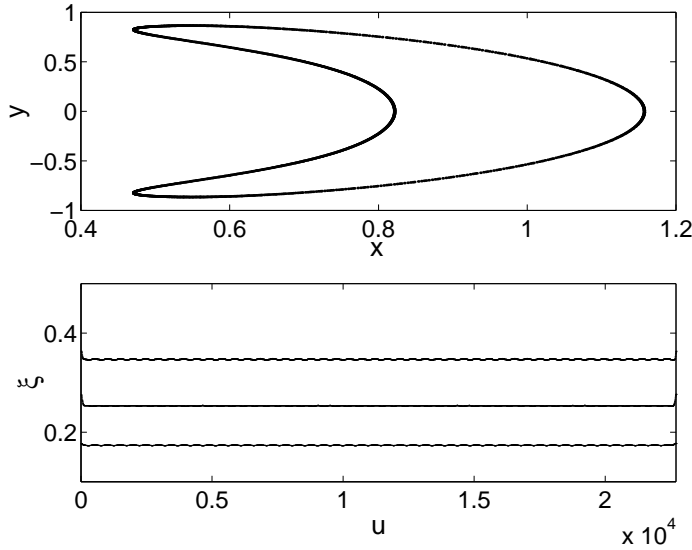


Fig. 7. Ridge plot of a quasiperiodic orbit of Hamiltonian (9) for  $F = 0.015$  and  $B = 0.3$  in the maximum configuration obtained for initial conditions  $(x, y) = (0.7, 0.5)$  in the Poincaré section. The upper part of the figure represents the Poincaré section of the trajectory.

oscillations are due to the interactions between ridges. This effect is explained in Appendix A. The frequency map analysis gives the following values for the first frequencies:  $\omega_1 = 0.1735$ ,  $\omega_2 = 0.2531$  and  $\omega_3 = 2\omega_1 = 0.3470$ .

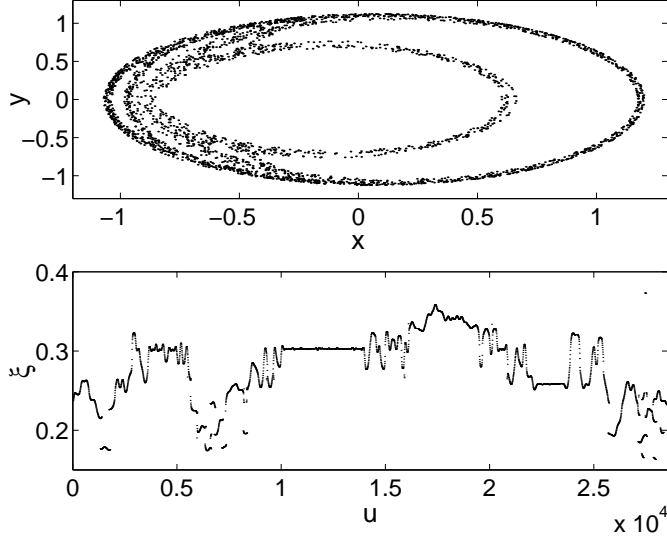


Fig. 8. Ridge plot of a chaotic orbit of Hamiltonian (9) for  $F = 0.015$  and  $B = 0.3$  in the maximum configuration obtained for initial conditions:  $(x, y) = (-0.5, 0.7)$ . The upper part of the figure represents the Poincaré section of the trajectory.

#### 4.2.3 Chaotic orbits: resonance trappings and transitions

We consider a trajectory in a chaotic region obtained for initial conditions  $(x, y) = (-0.5, 0.7)$  in the Poincaré section. Figure 8 depicts a Poincaré section of this trajectory and the ridge plot of the coordinate  $x(t)$  over the time interval  $[0, 2.85 \cdot 10^4]$  (with a ridge detection threshold  $\epsilon = 0.5$ ).

Figure 9 depicts an enlargement of the ridge plot of Fig. 8 on the time interval  $[1.35 \cdot 10^4, 2.65 \cdot 10^4]$  of two coordinates  $x$  and  $y$  with a smaller ridge detection threshold  $\epsilon = 0.1$ . Similar ridge plots are obtained with the other coordinates  $p_x$  and  $p_y$ .

Three different type of regimes are observed on these figures: trapping regions where the frequency is constant, weakly chaotic regions where the frequency is changing smoothly (for instance, from  $t = 1.6 \cdot 10^4$  to  $t = 1.95 \cdot 10^4$ ), and strongly chaotic regions characterized by many short ridges (for instance between  $t = 5.5 \cdot 10^3$  and  $t = 8.5 \cdot 10^3$ ).

The two main trapping regions in these figures are obtained from  $t = 10^4$  to  $t = 1.38 \cdot 10^4$  where the trajectory is trapped around the elliptic island surrounding the periodic orbit with frequency  $\omega_B$ , and from  $t = 2.23 \cdot 10^4$  to  $t = 2.35 \cdot 10^4$  where the trajectory is trapped around the elliptic island with frequency  $\omega_C$ .

The part of phase space visited by the trajectory is compact (this is due to the magnetic field) so we do not expect great variations of the main frequency.

In Fig. 10, we depict a resonance transition that occurs in the system for  $F = 0.02$  and  $B = 0.3$  (still in the maximum configuration) for initial conditions  $(x, y) = (-0.7, -0.5)$  in the Poincaré section. This figure displays the

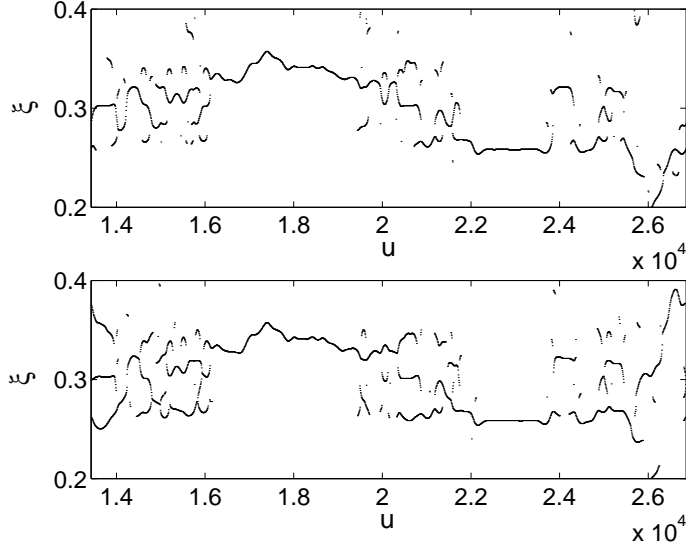


Fig. 9. Ridge plot of the chaotic orbit of Fig. 8 on the time interval  $[1.35 \cdot 10^4, 2.65 \cdot 10^4]$ . The upper part of the ridge plot is obtained by analyzing the coordinate  $x(t)$  and the lower part is the one for the coordinate  $y(t)$ .

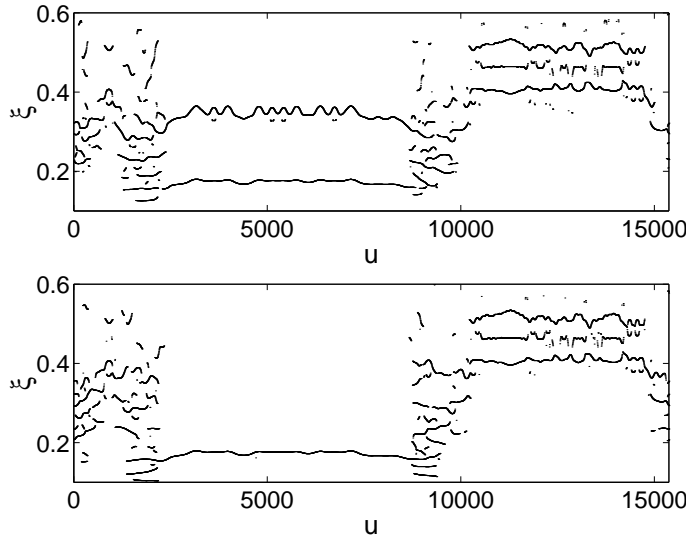


Fig. 10. Ridge plot of the chaotic orbit of Hamiltonian (9) in the maximum configuration with the parameters  $F = 0.02$  and  $B = 0.3$  obtained for initial conditions  $(x, y) = (-0.7, -0.5)$  in the Poincaré section. The upper part of the ridge plot is obtained by analyzing the coordinate  $x(t)$  and the lower part is obtained from the coordinate  $y(t)$ .

ridges of the coordinates  $x$  and  $y$  with a ridge detection threshold  $\epsilon = 0.1$ . There are two trapping regions: from  $t = 3000$  to  $t = 8000$  and from  $t = 10400$  to  $t = 14500$ . The first trapping region is characterized by two main frequencies  $\omega_1 = 0.1750$  and  $\omega_2 = 2\omega_1$ , and the second trapping region has three main frequencies  $\omega'_1 = 0.4106$ ,  $\omega'_2 = 0.4630$  and  $\omega'_3 = 2\omega_2 - \omega_1$ . Both regions are separated by a strongly chaotic region characterized by many short ridges

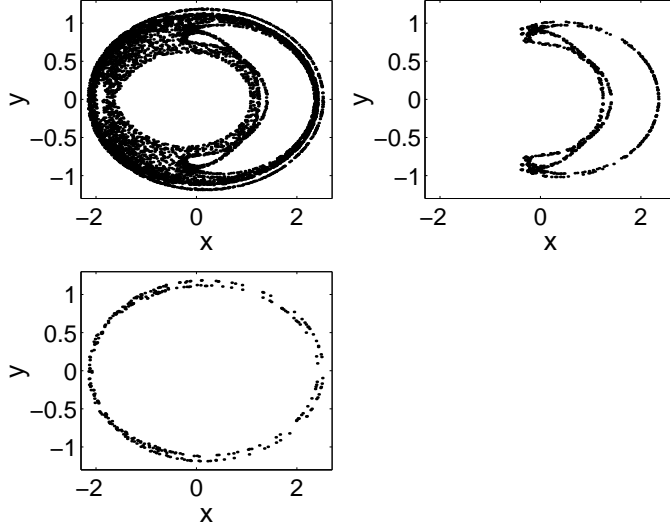


Fig. 11. Poincaré section of the trajectory of Fig. 10. The upper left panel is the trajectory from  $t = 0$  to  $t = 6.1 \cdot 10^4$ , the upper right panel is the trajectory from  $t = 3 \cdot 10^3$  to  $t = 8 \cdot 10^3$ , and the lower panel is the trajectory from  $t = 10.4 \cdot 10^3$  to  $t = 14.5 \cdot 10^3$ .

(resonance transition region). Figure 11 displays Poincaré section of the trajectory from  $t = 0$  to  $t = 61400$  (upper left panel), the section of this trajectory which is trapped between  $t = 3000$  and  $t = 8000$  (upper right panel), and the section of the trajectory trapped from  $t = 10400$  to  $t = 14500$  (lower panel). In the trapped regions, the trajectory nearly fills a one-dimensional part of the Poincaré surface.

From Figs. 9 and 10, we notice that the ridge plots are the same for the  $x$  coordinate of the  $y$  coordinate. The only difference is that a given ridge has different amplitudes according to whether it has been computed using  $x(t)$  or  $y(t)$ . One exception is Fig. 10 from  $t = 3000$  to  $t = 8000$ : only the ridges of sufficient amplitude are detected (with a ridge detection threshold  $\epsilon = 0.1$ ) and the ridge around  $\xi \approx 0.35$  which is the main ridge for the  $x$  coordinate has a low amplitude for the  $y$  coordinate. This ridge appears if we include low amplitude ridges in the detection.

The noticeable differences between the ridge plots for  $x$  and the ones for  $y$  are in the strong chaotic region where there are no elliptic islands and thus no trappings. In this regime which is the same as the one in Fig. 4 for the standard map, the significance of a frequency or a set of frequencies as an indicator is not clear. It means that the basis is not adapted to the strong chaotic regime. However, computing the ridge curves is useful since it provides a way to locate these strongly chaotic regions. It also provides a quantitative distinction between weak and strong chaos by looking at the number of short ridges.

We highlight that computing a single instantaneous frequency from the maximum wavelet coefficients can provide erroneous information. Figure 12 depicts the ridges in a strongly chaotic zone of phase space (the same trajectory as for

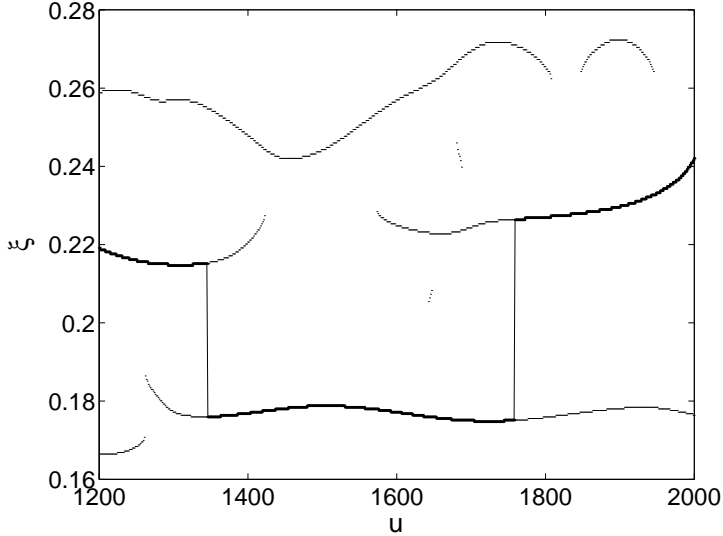


Fig. 12. Ridge plot of the same trajectory as for Fig. 8 on the time interval [1200, 2000]. The bold curve represents the main frequency curve.

Fig. 8 on the time interval [1200, 2000]). The bold curve is the main frequency ridge. By looking at this main frequency, we cannot say if the trajectory is in a strong chaotic region or if it sharply jumps between different trapping regions. The computation of secondary ridges shows that it is indeed a strongly chaotic zone without trappings.

#### 4.2.4 Time-frequency analysis of higher dimensional systems

The time-frequency analysis can be carried out for higher dimensional systems. We consider the elliptically polarized case with  $\alpha = 0.9$  represented by Hamiltonian (9) in the rotating frame. In this case,  $\tilde{p}_w$  is no longer a conserved quantity so Hamiltonian (9) has three degrees of freedom. Figure 13 depicts the ridge plot of the  $x$  coordinate with a ridge detection threshold  $\epsilon = 0.5$ , and Figure 14 depicts the ridge plot of the  $y$  coordinate with a ridge detection threshold  $\epsilon = 0.1$ .

We notice that from this figure the trajectory looks more chaotic than in the circularly polarized case which is in agreement with Refs. [23,24] (see the differences between Fig. 8 and Fig. 13). From Figs. 13 and 14, we detect resonance trappings and weakly chaotic regions. For instance, from  $t = 1.45 \cdot 10^4$  to  $t = 1.65 \cdot 10^4$  the trajectory is trapped in a region where the main frequencies are  $\omega_1 = 0.127$  (which is the main frequency for  $y$ ) and  $\omega_2 = 2\omega_1$  (which is the main frequency for  $x$ ). The same trapping is observed on a longer time interval from  $t = 2.65 \cdot 10^4$  to  $t = 3.15 \cdot 10^4$ . This is confirmed by a Fourier analysis of the segments of the trajectory: Figure 15 shows the power spectrum of two segments of the trajectory: from  $t = 1.45 \cdot 10^4$  to  $t = 1.65 \cdot 10^4$  which is expected to be close to quasiperiodic, and from  $t = 3.2 \cdot 10^4$  to  $t = 3.6 \cdot 10^4$

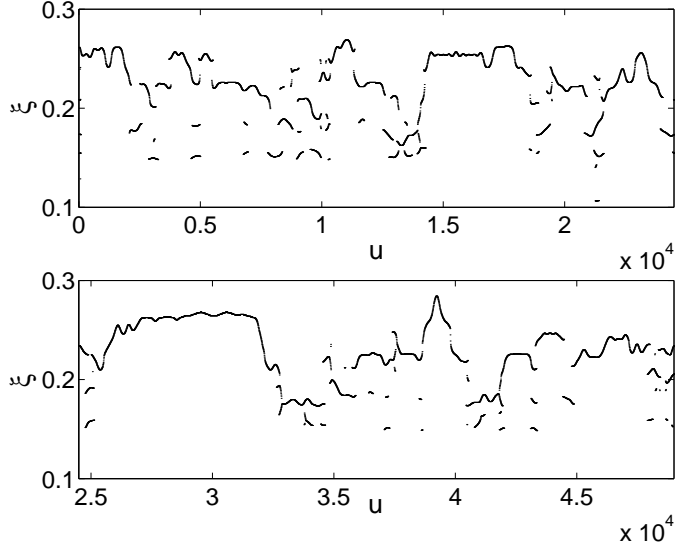


Fig. 13. Ridge plot of the  $x$  coordinate of the chaotic orbit of Hamiltonian (9) with  $\alpha = 0.9$  with the parameters  $F = 0.015$  and  $B = 0.3$  obtained for initial conditions  $(x, y) = (-0.5, 0.7)$  and  $p_w$  solution of Eq. (10);  $p_x$  and  $p_y$  are solution of  $\tilde{H}_{eff} = 0$  and  $xp_x + yp_y = 0$ . The upper part of the ridge plot is for the time interval  $[0, 2.4 \cdot 10^4]$  and the lower part is for  $[2.4 \cdot 10^4, 4.9 \cdot 10^4]$ . The ridge detection threshold is  $\epsilon = 0.5$ .

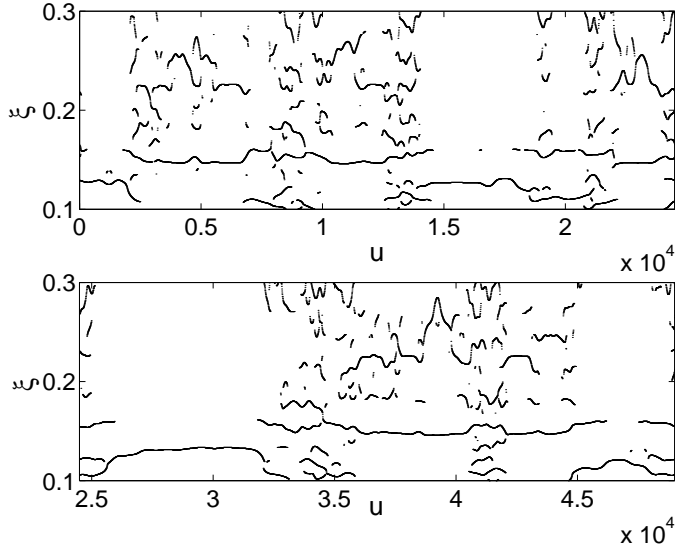


Fig. 14. Ridge plot of the  $y$  coordinate of the same trajectory as Fig. 13 with a ridge detection threshold  $\epsilon = 0.1$ .

which is expected to be strongly chaotic with a broad-band spectrum.

By increasing the ridge detection threshold (see Fig. 14), we clearly see the trapping regions (with one main flat ridge) and the strongly chaotic regions. We notice that there are regions where there is one main flat ridge with additional short ridges (for instance from  $t = 10^4$  to  $t = 1.25 \cdot 10^4$  or from  $t = 3.6 \cdot 10^4$  to  $t = 4 \cdot 10^4$ ). A Fourier analysis of these segments of trajectory shows a main



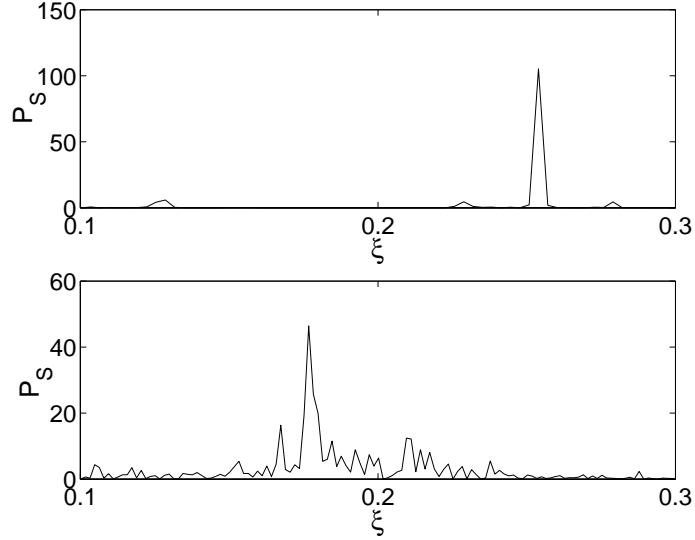


Fig. 15. Power spectrum of two segments of the trajectory of Fig 13 ( $x$  coordinate): from  $t = 1.45 \cdot 10^4$  to  $t = 1.65 \cdot 10^4$  (upper panel), and from  $t = 3.2 \cdot 10^4$  to  $t = 3.6 \cdot 10^4$  (lower panel).

frequency  $\omega \approx 0.15$  and a broad-band component. This is a nearly trapped region near some elliptic island. From Fig. 14, we notice that the trajectory is trapped in this island from  $t = 4.22 \cdot 10^4$  to  $t = 4.3 \cdot 10^4$ , and the main frequencies are  $\omega_1 = 0.15$  and  $\omega_2 = 0.22$ .

## 5 Conclusion

In summary, we showed how instantaneous frequencies based on a ridge extraction of a wavelet decomposition of a single trajectory coordinate reveal the phase space structures (resonance transitions, trappings, etc.) of chaotic systems. Our method also gives a quantitative characterization of weak and strong chaos through trappings and through the number of short ridges. We have showed that this time-frequency analysis can be carried out on trajectories of maps and flows. Note that nothing in our analysis depends on the dimensionality of the system: Given a time series (which can be e.g., one of the coordinates of the system whatever the number of such coordinates may be, or indeed data sets), we can compute the ridges of the time-frequency landscape, leading to the instantaneous frequencies. Moreover, the computational time is independent of the dimensionality of the system. The time-frequency method based on a single trajectory analysis is therefore very well suited for exploring phase space structures of various systems independently of the number of degrees of freedom.

## Acknowledgments

CC acknowledges useful discussions with N. Garnier and J. Laskar. This work was supported by the National Science Foundation and by ONR Grant No. N00014-01-1-0769.

## A Time-frequency analysis of quasiperiodic trajectories

Given the following quasiperiodic function

$$f(t) = e^{i\omega_1 t} + \sum_{k>1} a_k e^{i\omega_k t}, \quad (\text{A.1})$$

where  $a_k \in \mathbb{C}$ , we derive an approximation of the ridges of the time-frequency landscape obtained using the windowed Fourier transform and the continuous wavelet transform.

### A.1 Windowed Fourier transform

The windowed Fourier transform of trajectory (A.1) is (up to an overall constant  $\sigma\sqrt{2\pi}$ ):

$$Sf(u, \xi) = e^{i\omega_1 u} e^{-\sigma^2(\omega_1 - \xi)^2/2} + \sum_{k>1} a_k e^{i\omega_k u} e^{-\sigma^2(\omega_k - \xi)^2/2}.$$

We want to study the behavior of  $Sf(u, \xi)$  around  $\xi \approx \omega_1$ . We expand  $Sf(u, \xi)$  up to second order in the variable  $x = \xi - \omega_1$ :

$$Sf(u, \xi) = Sf^{(0)} + Sf^{(1)}x + Sf^{(2)}x^2 + O(x^3),$$

where

$$\begin{aligned} Sf^{(0)} &= e^{i\omega_1 u} + \sum_{k>1} a_k e^{i\omega_k u} e^{-\sigma^2(\omega_k - \omega_1)^2/2}, \\ Sf^{(1)} &= \sigma^2 \sum_{k>1} a_k (\omega_k - \omega_1) e^{i\omega_k u} e^{-\sigma^2(\omega_k - \omega_1)^2/2}, \\ Sf^{(2)} &= -\frac{1}{2} \sigma^2 \left\{ e^{i\omega_1 u} + \sum_{k>1} a_k [1 - \sigma^2(\omega_k - \omega_1)^2] e^{i\omega_k u} e^{-\sigma^2(\omega_k - \omega_1)^2/2} \right\}. \end{aligned}$$

The ridge around  $\omega_1$  is the local maximum of the absolute value of  $Sf(u, \xi)$  for each  $u$ . The expression of the spectrogram is

$$|Sf(u, \xi)|^2 = |Sf^{(0)}|^2 + 2\text{Re} \left( Sf^{(0)} Sf^{(1)*} \right) x \\ + \left[ 2\text{Re} \left( Sf^{(0)} Sf^{(2)*} \right) + |Sf^{(1)}|^2 \right] x^2 + O(x^3).$$

The ridge is approximately located at

$$\xi(u) = \omega_1 - \frac{\text{Re} \left( Sf^{(0)} Sf^{(1)*} \right)}{2\text{Re} \left( Sf^{(0)} Sf^{(2)*} \right) + |Sf^{(1)}|^2}.$$

When the terms  $a_k e^{-\sigma^2(\omega_k - \omega_1)^2/2}$  are small (compared to 1) which is the case when  $a_k$  is small or  $\omega_k$  is sufficiently far from  $\omega_1$ , the expression of the ridge becomes :

$$\xi(u) = \omega_1 + \sum_{k>1} (\omega_k - \omega_1) A_k \cos[(\omega_k - \omega_1)u + \phi_k] e^{-\sigma^2(\omega_k - \omega_1)^2/2}, \quad (\text{A.2})$$

where  $a_k = A_k e^{i\phi_k}$ . The instantaneous frequency curve is again a quasiperiodic function with frequencies  $\omega_k - \omega_1$ . It oscillates around the main frequency  $\omega_1$  with amplitude proportional to  $e^{-\sigma^2(\omega_k - \omega_1)^2/2}$ . These oscillations can be reduced by increasing the length of the window of the transform  $\sigma$ .

## A.2 Wavelet transform

The wavelet transform of trajectory (A.1) is (up to an overall constant  $\sigma\sqrt{2\pi}$ ):

$$Wf(u, s) = e^{i\omega_1 u} e^{-\sigma^2 s^2 (\omega_1 - \eta/s)^2/2} + \sum_{k>1} a_k e^{i\omega_k u} e^{-\sigma^2 s^2 (\omega_k - \eta/s)^2/2}.$$

We want to study the behavior of the normalized scalogram  $P_W f(u, \xi)$  around  $s \approx \eta/\omega_1$ . We expand  $s^{-1/2} Wf(u, s)$  up to second order in the variable  $x = s\omega_1/\eta - 1$  :

$$s^{-1/2} Wf(u, s) = Wf^{(0)} + Wf^{(1)}x + Wf^{(2)}x^2 + O(x^3),$$

where

$$Wf^{(0)} = e^{i\omega_1 u} + \sum_{k>1} a_k e^{i\omega_k u} e^{-\sigma^2 \eta^2 (\omega_k/\omega_1 - 1)^2/2}, \\ Wf^{(1)} = -\sigma^2 \eta^2 \sum_{k>1} a_k \frac{\omega_k}{\omega_1} \left( \frac{\omega_k}{\omega_1} - 1 \right) e^{i\omega_k u} e^{-\sigma^2 \eta^2 (\omega_k/\omega_1 - 1)^2/2}, \\ Wf^{(2)} = -\frac{1}{2} \sigma^2 \eta^2 \left\{ e^{i\omega_1 u} + \sum_{k>1} a_k \frac{\omega_k^2}{\omega_1^2} \left[ 1 - \sigma^2 \eta^2 \left( \frac{\omega_k}{\omega_1} - 1 \right)^2 \right] e^{i\omega_k u} e^{-\sigma^2 \eta^2 (\omega_k/\omega_1 - 1)^2/2} \right\}.$$

The ridge around  $\omega_1$  is given by the local maximum of  $P_W f(u, \xi)$  for each  $u$ . The expression of the normalized scalogram

$$\begin{aligned} \frac{1}{s}|Wf(u, s)|^2 &= |Wf^{(0)}|^2 + 2\operatorname{Re}\left(Wf^{(0)}Wf^{(1)*}\right)x \\ &\quad + \left[2\operatorname{Re}\left(Wf^{(0)}Wf^{(2)*}\right) + |Wf^{(1)}|^2\right]x^2 + O(x^3). \end{aligned}$$

The ridge is approximately located at

$$\xi(u) = \omega_1 - \frac{\operatorname{Re}\left(Wf^{(0)}Wf^{(1)*}\right)}{2\operatorname{Re}\left(Wf^{(0)}Wf^{(2)*}\right) + |Wf^{(1)}|^2}.$$

When the terms  $a_k e^{-\sigma^2 \eta^2 (\omega_k / \omega_1 - 1)^2 / 2}$  are small (compared to 1) which is the case when  $a_k$  is small or  $\omega_k$  is sufficiently far from  $\omega_1$ , the expression of the ridge becomes :

$$\xi(u) = \omega_1 + \sum_{k>1} \omega_k (\omega_k / \omega_1 - 1) A_k \cos[(\omega_k - \omega_1)u + \phi_k] e^{-\sigma^2 \eta^2 (\omega_k / \omega_1 - 1)^2 / 2}. \quad (\text{A.3})$$

As for the windowed Fourier transform, the instantaneous frequency is a quasiperiodic function with frequencies  $\omega_k - \omega_1$ . It oscillates around the main frequency  $\omega_1$ . The amplitude of the oscillations is proportional to  $e^{-\sigma^2 \eta^2 (\omega_k / \omega_1 - 1)^2 / 2}$ . They can be reduced by increasing the parameters of the wavelet  $\sigma$  and  $\eta$ .

## B Effect of finite time

In this section, we investigate the effect of the finite time on the computation of the instantaneous frequencies. We consider the signal  $f(t) = e^{i\omega t}$  on  $[0, T]$ .

### B.1 Windowed Fourier transform

The windowed Fourier transform is computed by considering a periodic signal  $\tilde{f}$  with period  $T$  constructed from  $f$ , i.e.  $\tilde{f}(t) = f(t)$  for  $t \in [0, T[$  and  $\tilde{f}(t + T) = \tilde{f}(t)$  for all  $t$ . However the signal  $\tilde{f}$  may not be continuous if the value of the original signal  $f$  at 0 and  $T$  are not the same. The discontinuities lead to an alteration of the instantaneous frequencies near these points.

We compute the ridge near a point of discontinuity, e.g.,  $u = 0$ . The windowed Fourier transform of  $\tilde{f}$  is equal to

$$S\tilde{f}(u, \xi) = (\sigma^2 \pi)^{-1/4} \sum_{n=-\infty}^{+\infty} \int_{nT}^{(n+1)T} \tilde{f}(t) e^{-i\xi t} e^{-(t-u)^2 / (2\sigma^2)} dt.$$

For  $u$  close to zero, two terms are predominant in the sum:  $n = -1$  and  $n = 0$ . On the interval  $[-T, 0]$ , the function  $\tilde{f}$  is equal to  $e^{i\omega(t+T)}$ . Thus

$$(\sigma^2\pi)^{1/4}S\tilde{f}(u, \xi) \approx \int_0^T e^{i(\omega-\xi)t} e^{-(t-u)^2/(2\sigma^2)} dt + e^{i\omega T} \int_0^T e^{-i(\omega-\xi)t} e^{-(t+u)^2/(2\sigma^2)} dt.$$

We introduce the error function  $\operatorname{erf}(z) = \frac{2}{\sqrt{\pi}} \int_0^z e^{-t^2} dt$ :

$$\begin{aligned} S\tilde{f}(u, \xi) &= \left(\frac{\sigma^2\pi}{4}\right)^{1/4} e^{i(\omega-\xi)u} e^{-\sigma^2(\omega-\xi)^2/2} \\ &\quad \times \left[ \operatorname{erf}\left(\frac{T-u-i\sigma^2(\omega-\xi)}{\sigma\sqrt{2}}\right) + \operatorname{erf}\left(\frac{u+i\sigma^2(\omega-\xi)}{\sigma\sqrt{2}}\right) \right] \\ &+ e^{i\omega T} \left(\frac{\sigma^2\pi}{4}\right)^{1/4} e^{i(\omega-\xi)u} e^{-\sigma^2(\omega-\xi)^2/2} \\ &\quad \times \left[ \operatorname{erf}\left(\frac{T+u+i\sigma^2(\omega-\xi)}{\sigma\sqrt{2}}\right) + \operatorname{erf}\left(\frac{-u-i\sigma^2(\omega-\xi)}{\sigma\sqrt{2}}\right) \right] \end{aligned}$$

We assume that  $T$  is large compared to  $u$  and  $\sigma^2|\omega - \xi|$ . We introduce the complex error function  $w(z)$  as  $w(z) = e^{-z^2}[1 + \operatorname{erf}(iz)]$  (see Ref. [25]). Since  $\operatorname{erf} z \rightarrow 1$  when  $z \rightarrow \infty$  and  $|\arg z| < \pi/4$ , the expression of the windowed Fourier transform becomes:

$$S\tilde{f}(u, \xi) \approx \left(\frac{\sigma^2\pi}{4}\right)^{1/4} e^{-y^2} [w(x+iy) + e^{i\omega T} w(-x-iy)],$$

where  $x = \sigma(\omega - \xi)/\sqrt{2}$  and  $y = -u/(\sigma\sqrt{2})$ . We notice that when  $\omega T = 0 \pmod{2\pi}$ , the expression of  $S\tilde{f}$  becomes equal to

$$S\tilde{f}(u, \xi) \approx (4\pi\sigma^2)^{1/4} e^{iu(\omega-\xi)} e^{-\sigma^2(\omega-\xi)^2/2},$$

since  $w(z) + w(-z) = 2e^{-z^2}$ . That is the windowed Fourier transform of the periodic signal  $e^{i\omega t}$  on  $\mathbb{R}$ . When  $\omega T \neq 0 \pmod{2\pi}$ , the ridge is no longer constant and located at  $\xi = \omega$ , the discontinuity distorts locally the ridge.

We first consider  $u = 0$  for simplicity. Using the following development of the error function,

$$w(z) = 1 + \frac{2i}{\sqrt{\pi}}z - z^2 - \frac{4i}{3\sqrt{\pi}}z^3 + \frac{z^4}{2} + \dots,$$

we obtain the following expansion for the spectrogram:

$$\begin{aligned} P_S\tilde{f}(0, \xi) &= 2(1 + \cos \omega T) + x \frac{8}{\sqrt{\pi}} \sin \omega T - 4x^2 \left[ 1 - \frac{2}{\pi} + \left(1 + \frac{2}{\pi}\right) \cos \omega T \right] \\ &\quad - x^3 \frac{40}{3\sqrt{\pi}} \sin \omega T + 4x^4 \left[ 1 - \frac{8}{3\pi} + \left(1 + \frac{8}{3\pi}\right) \cos \omega T \right] + \dots, \end{aligned}$$

where we have dropped the overall constant  $\sigma\sqrt{\pi}/2$ . The equation that determines the extrema of the spectrogram at  $u = 0$  is the following one:

$$\begin{aligned} \frac{1}{\sqrt{\pi}} \sin \omega T - x \left[ 1 - \frac{2}{\pi} + \left( 1 + \frac{2}{\pi} \right) \cos \omega T \right] - x^2 \frac{5}{\sqrt{\pi}} \sin \omega T \\ + 2x^3 \left[ 1 - \frac{8}{3\pi} + \left( 1 + \frac{8}{3\pi} \right) \cos \omega T \right] + \dots = 0 \end{aligned} \quad (\text{B.1})$$

From a solution  $x_0$  of this equation, we obtain an approximation of the ridge:

$$\xi = \omega - \frac{\sqrt{2}}{\sigma} x_0.$$

One of the main features of a solution  $x_0$  of this equation is that it does not depend on how large is the time interval. It only depends on the fractional part of  $\omega T/(2\pi)$ . Moreover this error decreases like  $1/\sigma$  as  $\sigma$  is increased. Again we notice that when  $\omega T = 0 \pmod{2\pi}$  the ridge is located at  $\xi = \omega$ .

We neglect the quadratic and cubic term of Eq. (B.1) which is valid if  $\theta \equiv \omega T \pmod{2\pi}$  is close to zero. There is only one ridge at  $u = 0$  which is approximately located at

$$\xi = \omega - \frac{1}{\sigma\sqrt{2\pi}} \sin \omega T.$$

The ridge is above  $\xi = \omega$  when  $\theta$  is negative, and below  $\xi = \omega$  when  $\theta$  is positive.

When  $\omega T = \pi \pmod{2\pi}$ , there is an extremum at  $x_0 = 0$ . However this solution is a minimum of the spectrogram. By considering the quartic term in the equation, we see that there are two other local minimum given by:

$$\xi_{\pm} = \omega \pm \frac{\sqrt{3}}{2\sigma}.$$

Both ridges are local maxima of the spectrogram.

When the quadratic term of the expansion of the spectrogram vanishes (for  $\omega T \approx 1.7947 \pmod{2\pi}$ ), Eq. (B.1) shows that there are two extrema for the spectrogram:

$$\xi_{\pm} = \omega \pm \frac{1}{\sigma} \sqrt{\frac{5}{2}}.$$

Only  $\xi_-$  is a local maximum of the spectrogram and is located below  $\xi = \omega$ .

We compute next an approximation of the ridge when  $u$  is increased. Using the expansion of  $w$ , we obtain

$$\begin{aligned} P_S \tilde{f}(u, \xi) = P_S \tilde{f}(0, \xi) - 4x^2 y^2 \left[ 1 + \frac{2}{\pi} + \left( 1 - \frac{2}{\pi} \right) \cos \omega T \right] \\ + x^3 y^2 \frac{40}{3\sqrt{\pi}} \sin \omega T + 4x^4 y^2 \left[ 1 - \frac{8}{3\pi} + \left( 1 + \frac{8}{3\pi} \right) \cos \omega T \right] \\ + O(y^4, x^5), \end{aligned}$$

The equation that determines the ridge is the following one:

$$\begin{aligned} & \frac{1}{\sqrt{\pi}} \sin \omega T - x \left[ 1 - \frac{2}{\pi} + \left( 1 + \frac{2}{\pi} \right) \cos \omega T \right] - xy^2 \left[ 1 + \frac{2}{\pi} + \left( 1 - \frac{2}{\pi} \right) \cos \omega T \right] \\ & - x^2(1-y^2) \frac{5}{\sqrt{\pi}} \sin \omega T + 2x^3(1+y^2) \left[ 1 - \frac{8}{3\pi} + \left( 1 + \frac{8}{3\pi} \right) \cos \omega T \right] + \dots = 0 \end{aligned}$$

The approximation of the ridge is given by

$$\xi(u) = \omega - \frac{1}{\sigma\sqrt{2\pi}} \left( 1 - \frac{u^2}{2\sigma^2} \right) \sin \omega T.$$

The ridge decreases (or increases) with  $u$  if the ridge is above (resp. below) the main frequency  $\omega$ . The time interval where the effect of the discontinuity at  $u = 0$  is visible is approximately  $[0, \tau]$  where

$$\tau = \sigma\sqrt{2}.$$

The length of this interval is independent of the total time length  $T$  and is proportional to  $\sigma$ . If we increase  $\sigma$ , the difference between the ridge and the frequency  $\omega$  decreases as  $1/\sigma$  but the time interval where this effect is visible increases as  $\sigma$ . Figure B.1 displays the ridge plots in three cases: The first panel is for  $\theta = 0$  where a flat ridge is expected, the second panel is for  $\theta = \pi/4$  and  $\sigma = 1$ , and the third panel is for  $\theta = \pi/4$  and  $\sigma = 1.5$ .

For  $\omega T = \pi \pmod{2\pi}$ , the extremum  $x = 0$  is a minimum for  $y$  small and becomes a maximum for  $y > 1$ . Thus the typical time of the effect of the discontinuity is again  $\tau = \sigma\sqrt{2}$ . For  $y < 1$ , there are two ridges approximately located at :

$$\xi_{\pm}(u) = \omega \pm \frac{\sqrt{3}}{2\sigma} \left( 1 - \frac{u^2}{2\sigma^2} \right).$$

These two ridges are symmetric with respect to  $\xi(u) = \omega$ . Figure B.2 displays the two ridges in that case. The asymmetry on this figure is due to the correction of higher order terms in  $x$  in the expansion of the spectrogram.

## B.2 Wavelet transform

The effect of a discontinuity at  $u = 0$  due to a periodisation is approximately the same as for the windowed Fourier transform. The computations are very similar. The wavelet transform of  $\tilde{f}$  is given by

$$W\tilde{f}(u, s) = (\sigma^2\pi)^{-1/4} \frac{1}{\sqrt{s}} \sum_{n=-\infty}^{+\infty} \int_{nT}^{(n+1)T} \tilde{f}(t) e^{-i\eta(t-u)/s} e^{-(t-u)^2/(2s^2\sigma^2)} dt.$$

Again two terms are important in the sum  $n = -1$  and  $n = 0$ .

$$e^{-i\omega\eta/s} \sqrt{s}(\sigma^2\pi)^{1/4} W\tilde{f}(u, s) \approx \int_0^T e^{i(\omega-\eta/s)t} e^{-(t-u)^2/(2s^2\sigma^2)} dt \\ + e^{i\omega T} \int_0^T e^{-i(\omega-\eta/s)t} e^{-(t+u)^2/(2s^2\sigma^2)} dt.$$

Next we assume that  $T$  is large and we express the wavelet transform using the complex error function  $w$ :

$$W\tilde{f}(u, s) \approx \left(\frac{\sigma^2\pi}{4}\right)^{1/4} e^{-y^2} \left[ w(x + iy) + e^{i\omega T} w(-x - iy) \right],$$

where  $x = \sigma(s\omega - \eta)/\sqrt{2}$  and  $y = -u/(s\sigma\sqrt{2})$ . The main difference with the windowed Fourier case is that now  $y$  depends on the frequency (through the scale). For  $\sigma\eta$  sufficiently large and  $s$  sufficiently close to  $\eta/\omega$ , we get an approximation of  $x$  and  $y$ :

$$x \approx \frac{\sigma\eta}{\omega\sqrt{2}}(\omega - \xi), \\ y \approx -\frac{\omega}{\sigma\eta\sqrt{2}}u,$$

where  $\xi = \eta/s$ . Thus the results of the windowed Fourier transform can be transposed for the wavelet transform by replacing  $\sigma$  by  $\sigma\eta/\omega$ .

Using the expansion of the error function, we obtain an approximation of the value of the maximum of the wavelet coefficients and hence an approximation of the ridge. For  $u = 0$  and for  $\omega T \approx 0 \pmod{2\pi}$ , this value is :

$$\xi = \omega - \frac{\omega}{\sigma\eta\sqrt{2\pi}} \sin \omega T.$$

In the case of the wavelet ridge, we notice that the difference is proportional to the frequency, i.e. the error in determining the frequency  $\omega$  will be smaller for low frequencies than for large ones.

For  $u$  close to zero, we get an approximation of the ridge:

$$\xi(u) = \omega - \frac{\omega}{\sigma\eta\sqrt{2\pi}} \left( 1 - \frac{u^2\omega^2}{2\sigma^2\eta^2} \right) \sin \omega T.$$

The typical width in time of the error in determining the frequency  $\omega$  is given by

$$\tau \approx \frac{\sigma\eta\sqrt{2}}{\omega}.$$

We notice that increasing the parameters of the wavelet decrease the amplitude of the error but increases the typical length time where this error is visible.

The wavelet method cannot determine frequencies such that  $\tau \geq T/2$ , i.e. frequencies such that

$$\omega \leq 2\sqrt{2}\frac{\sigma\eta}{T}$$



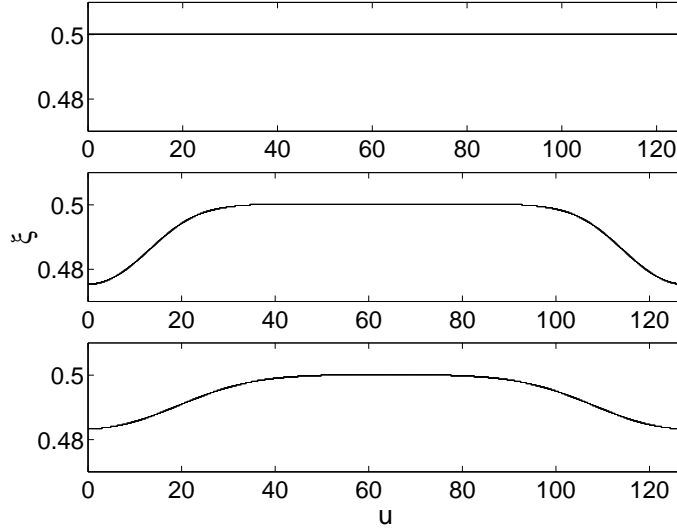


Fig. B.1. Wavelet ridge of a function  $f(t) = e^{i\omega t}$  with  $\omega = 1/2$  on an interval  $[0, T]$  for (a)  $\omega T = 20\pi$ , (b)  $\omega T = 20\pi + \pi/4$  and  $\sigma = 1$ , and (c)  $\omega T = 20\pi + \pi/4$  and  $\sigma = 1.5$ .

In summary, the fact that the trajectory is known on a finite time interval creates in general a discontinuity on the boundaries of this interval. This distorts the ridge on a small time interval. It creates one or two ridges; when there are two ridges, it means that the main original ridge is a minimum of the spectrogram. When there is one ridge, it can be below or above the main ridge depending on the value of the fractional part of  $\omega T/(2\pi)$ . We have seen that the amplitude of this distortion is inversely proportional to the size of the window of the Fourier transform and that the typical time interval during which this distortion is visible is proportional to this size of the window.

Figure B.3 represents the influence of the discontinuity in the time-frequency plane. The gray region is the portion of the time-frequency plane that has to be discarded due to the influence of the discontinuity on the boundaries. For the windowed Fourier transform, this error does not depend on the frequency whereas for the wavelet transform, the distortion influences greatly the low frequencies.

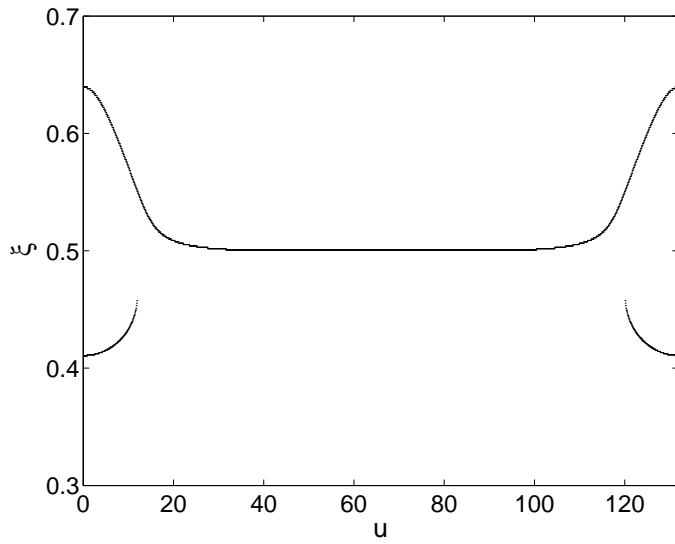


Fig. B.2. Wavelet ridge of a function  $f(t) = e^{i\omega t}$  with  $\omega = 1/2$  on an interval  $[0, T]$  for  $\omega T = 20\pi + \pi$ .

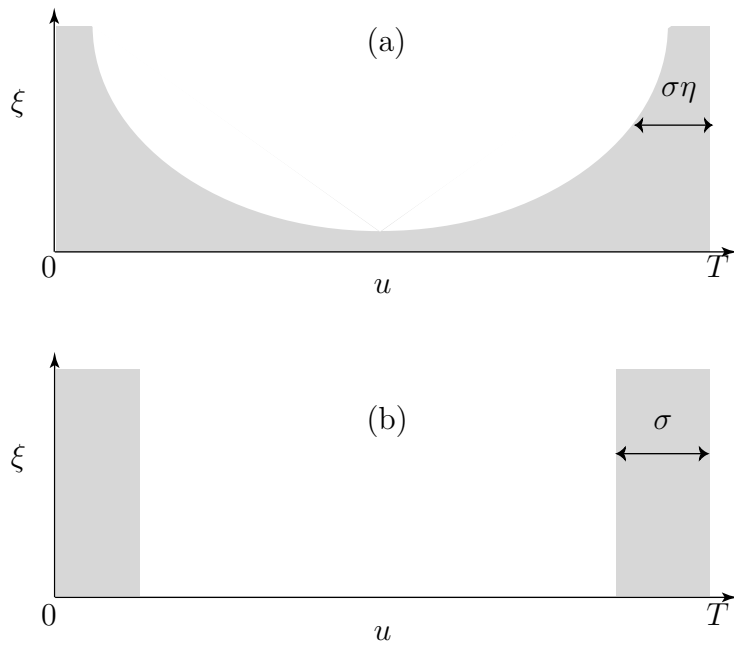


Fig. B.3. Schematic representation of the finite time effect on the computation of the ridges: The gray region is the part of the time-frequency plane where the discontinuity of the signal between  $t = 0$  and  $t = T$  influences the computation of the instantaneous frequencies (a) for the wavelet transform and (b) for the windowed Fourier transform.

## References

- [1] C.C. Martens, M.J. Davis, and G.S. Ezra. Local frequency analysis of chaotic motion in multidimensional systems: Energy transport and bottlenecks in planar OCS. *Chem. Phys. Lett.*, 142:519 – 528, 1987.
- [2] J. von Milczewski and T. Uzer. Mapping multidimensional intramolecular dynamics using frequency analysis. In D.L. Thompson, editor, *Modern Methods for Multidimensional Dynamics Computations in Chemistry*, pages 190 – 200, Singapore, 1998. World Scientific.
- [3] J. Laskar. The chaotic behavior of the solar system: A numerical estimate of the chaotic zones. *Icarus*, 88:266–291, 1990.
- [4] J. Laskar. Introduction to frequency map analysis. In C. Simó, editor, *Hamiltonian Systems with Three or More Degrees of Freedom*, NATO ASI Series, pages 134 – 150. Kluwer Academic Publishers, Dordrecht, 1999.
- [5] A. Correia and J. Laskar. The four final rotation states of Venus. *Nature*, 411:767 – 770, 2001.
- [6] D. Robin, C. Steier, J. Laskar, and L. Nadolski. Global dynamics of the advanced light source revealed through experimental frequency map analysis. *Phys. Rev. Lett.*, 85:558 – 561, 2000.
- [7] J. Laskar. Frequency analysis for multi-dimensional systems. Global dynamics and diffusion. *Physica D*, 67:257, 1993.
- [8] T.A. Michtchenko and D. Nesvorny. Wavelet analysis of the asteroidal resonant motion. *Astron. Astrophys.*, 313:674 – 678, 1996.
- [9] A. Askar, A.E. Cetin, and H. Rabitz. Wavelet transform for the analysis of molecular dynamics. *J. Phys. Chem.*, 100:19165, 1996.
- [10] L.V. Vela-Arevalo and S. Wiggins. Time-frequency analysis of classical trajectories of polyatomic molecules. *Int. J. Bifurcat. Chaos*, 11:1359 – 1380, 2001.
- [11] N. Delprat, B. Escudié, P. Guillemain, R. Kronland-Martinet, P. Tchamitchian, and B. Torrèsani. Asymptotic wavelet and Gabor analysis: Extraction of instantaneous frequencies. *IEEE Trans. Inform. Theory*, 38:644 – 664, 1992.
- [12] S. Mallat. *A wavelet tour of signal processing*. Academic Press, San Diego, 1999.
- [13] R. Carmona, W.-L. Hwang, and B. Torrèsani. *Practical Time-Frequency Analysis*. Acad. Press, San Diego, 1998.
- [14] N. Hess-Nielsen and M.V. Wickerhauser. Wavelets and time-frequency analysis. *Proc. IEEE*, 84:523 – 540, 1996.

- [15] N.E. Huang, Z. Shen, S.R. Long, M.C. Wu, H.H. Shih, Q. Zheng, N.-C. Yen, C.C. Tung, and H.H. Liu. The empirical mode decomposition and the Hilbert spectrum for nonlinear and non-stationary time series analysis. *Proc. R. Soc. Lond. A*, 454:903 – 995, 1998.
- [16] <http://www-stat.stanford.edu/~wavelab>. J.B. Buckheit and D.L. Donoho. Wavelab and reproducible research. In A. Antoniadis and G. Oppenheim, editors, *Wavelets and Statistics*. Springer-Verlag, Berlin, 1995.
- [17] H. Friedrich. *Theoretical Atomic Physics*. Springer-Verlag, Berlin, 1991.
- [18] E. Lee, A.F. Brunello, and D. Farrelly. Coherent states in a Rydberg atom: Classical mechanics. *Phys. Rev. A*, 55:2203 – 2221, 1997.
- [19] C. Chandre, D. Farrelly, and T. Uzer. Thresholds to chaos and ionization for the hydrogen atom in rotating fields. *Phys. Rev. A*, 65:053402, 2002.
- [20] D. Delande. Chaos in atomic and molecular physics. In M.J. Giannoni, A. Voros, and J. Zinn-Justin, editors, *Chaos and Quantum Physics*, Les Houches, Session LII, 1989, pages 665 – 726. Elsevier, 1991.
- [21] J. Laskar, C. Froeschlé, and A. Celletti. The measure of chaos by numerical analysis of the fundamental frequencies. application to the standard mapping. *Physica D*, 56:253–269, 1992.
- [22] B.V. Chirikov. A universal instability of many-dimensional oscillator systems. *Phys. Rep.*, 52:263–379, 1979.
- [23] E. Oks and T. Uzer. Ionization of hydrogen atom in elliptically polarized microwave field. *J. Phys. B: At. Mol. Opt. Phys.*, 32:3601 – 3613, 1999.
- [24] M.R.W. Bellermand, P.M. Koch, and D. Richards. Resonant, elliptical-polarization control of microwave ionization of hydrogen atom. *Phys. Rev. Lett.*, 78:3840 – 3843, 1997.
- [25] M. Abramowitz and I.A. Stegun. *Handbook of Mathematical Functions*. Dover, New York, 1964.